


REGULAR PAPER

# Vorticity dynamics diagnosis of the internal flow field in a high-load counter-rotating compressor

T. Yan, H. Chen and P. Yan 

School of Energy Science and Engineering, Harbin Institute of Technology, Harbin, China

Corresponding author: P. Yan; Email: [peigang\\_y@163.com](mailto:peigang_y@163.com)

Received: 1 February 2023; Revised: 12 April 2023; Accepted: 18 April 2023

**Keywords:** counter-rotating compressor; numerical simulation; vorticity dynamics diagnosis; boundary enstrophy flux; aerodynamic optimisation design

## Abstract

A high-load counter-rotating compressor is optimised based on the method of coupling aerodynamic optimisation technology and computational fluid dynamics, and the flow structures in the passage are analysed and evaluated by vorticity dynamics diagnosis. The results show that the aerodynamic performance of optimised compressor are obviously improved at both design point and off-design point. By comparing the distribution characteristics of vorticity dynamics parameters on the blade surface before and after the optimisation, it is found that BVF (boundary vorticity flux) and circumferential vorticity can effectively capture high flow loss regions such as shock waves and secondary flow in the passage. In addition, the BEF (Boundary enstrophy flux) diagnosis method based on the theory of boundary enstrophy flux is developed, which expands the application scenario of the boundary vorticity dynamics diagnosis method. The change of vorticity dynamics parameters shows blade geometric parameters' influence on the passage's viscous flow field, which provides a theoretical basis for the aerodynamic optimisation design.

## Nomenclature

$\omega$	vorticity (1/s)
$n$	normal vector
$\rho$	density ( $\text{kg/m}^3$ )
$\mu$	dynamics viscosity coefficient (Pa·s)
$T$	total pressure ratio
$P^*$	total pressure (Pa)
$T^*$	total temperature (K)
$\dot{m}$	rate of flow (kg/s)
$\eta^*$	efficiency
$\pi$	total pressure ratio
BVF	boundary vorticity flux ( $\text{m/s}^2$ )
BEF	boundary enstrophy flux ( $\text{kg/s}^3$ )
$\omega_\theta$	circumferential vorticity (1/s)

## 1.0 Introduction

The high-load counter-rotating compressor has obvious advantages in reducing the number of stages and improving the thrust-to-weight ratio of the aero-engine. However, with the increase of stage load, there are all kinds of complex vortices movement and flow separation problems in its high adverse-pressure-gradient passage, such as shock wave/boundary layer interaction, secondary flow, and other three-dimensional viscous fluid motion directly restrict the efficient and stable operation of

counter-rotating compressor [1–3]. With the development of computational fluid dynamics, the flow field details inside the turbomachinery passage are shown more comprehensively. It has become one of the important means to improve the aerodynamic performance of turbomachinery to remodel the high flow loss area based on the simulation results of flow field [4–8]. At present, the conventional simulation analysis methods usually diagnose the distribution of pressure and velocity to judge the quality of the flow field. However, the flow parameters such as pressure and velocity in most of the flow fields are basically continuously changing, and the qualitative analysis of such conventional physical quantities is limited in guiding the actual flow diagnosis and design optimisation of turbomachinery.

Küchemann and Lu pointed out that the vortex is the tendon of fluid motion and the essence of fluid is the vortex [9]. In the industrial application of turbomachinery, it is difficult to trace and measure the vortices movement in the flow field because of the complex geometric structure of the flow passage components. In order to study the underlay dynamics mechanism of vortices movement in fluid, including the generation, development, dissipation of vortices and the interaction between vortices, and analyse the correspondence rules among vortex structure, turbomachinery channel geometry and aerodynamic performance, it is necessary to analyse vorticity dynamics flow field diagnosis method [10–12]. Vortex dynamics diagnosis improves the shortcomings of conventional flow field analysis methods that are not intuitive enough to quickly give accurate suggestions of diagnosis and optimisation. At present, the development of vorticity dynamics has been relatively mature. Vorticity dynamics is based on fluid dynamics, which further studies the shear flow of fluid and the interaction between the shear effect and the bulging-pressing effect. It not only inherits the analysis method for flow field structure under the conventional framework of  $(v, p)$  – velocity and pressure – but also explores the changes and interactions of complex phenomena of separated flow in the channel under the framework of  $(\omega, \Pi)$  – vorticity and bulge pressure variable.

A large number of research results show that the vorticity dynamics diagnosis method can effectively predict the strength of shock wave and secondary flow in the passage of turbomachinery, capture and amplify the root of non-performing flow, which provides the accurate diagnostic basis for separated flow loss and three-dimensional optimisation of blade [13–15]. The vorticity moment theory proposed by Wu explains that the forces and moments in the fluid can be expressed as the integral of the first-order moment and the second-order moment of vorticity, respectively, from the perspective of vorticity. Vorticity is not only the source of lift but also the source of resistance. The forces and moments of the object can be improved by exerting favourable vortex and restraining harmful vortex [16–18]. Lambert et al. [19] proposed a vortex tracking method to obtain the vortex structure and its development process in laminar separation bubbles, which provided a solution for the exploration of vorticity dynamics in laminar separation bubbles. Wu et al. [20–23] proposed a dynamics diagnosis method of boundary vorticity flux (BVF) and successfully applied it in the field of aerodynamic performance optimisation and internal flow analysis of turbomachinery, providing a theoretical basis and technical support for realising highly efficient energy conversion. The results show that the wall is the source of vorticity generation and diffusion to the fluid, and the flow separation in the boundary layer can be suppressed to the greatest extent by controlling the area of BVF positive peak distribution on the blade surface that causes undesirable performance. Li et al. [24, 25] introduced the BVF theory into the research of aerodynamic performance optimisation for compressor, the results show that the distribution characteristics of BVF on the blade surface are beneficial to predict the accumulation of low-energy fluid in the boundary layer, which is of guiding significance to improve the fluid flow condition and mechanical characteristics in the passage. Li et al. [26] directly took the distribution of BVF positive peak on the blade surface as the optimisation objective to optimise the flow field structure and aerodynamic performance of a low-speed compressor. After optimisation, the flow loss in the compressor passage was significantly reduced, and the efficiency and stability of the compressor were improved. Prashanth et al. [27] used the numerical simulation method to study the vorticity dynamics of the tip leakage vortex of a transonic fan and analysed the formation reasons of leakage vortex and its influence on the flow field. Yang et al. [28, 29] applied vorticity dynamics diagnosis to the three-dimensional geometry optimisation of hydraulic turbines blade, discussed the mathematical relationship between blade geometry and vorticity

dynamics parameters and verified the applicability of vorticity dynamics in the application of hydraulic turbines. Fan et al. [30] respectively used the flow section diagnosis method and the BVF diagnosis method to analyse the vorticity dynamics of the turbine runner, which is of certain reference significance for the runner design.

It is worth noting that the above research on vorticity dynamics diagnosis methods are only limited to the flow field diagnosis and design optimisation of single-row blades, and the flow field diagnosis of multi-row blades with the complex geometry of counter-rotating compressors has not been carried out. The research of this paper is helpful to explore the application of vorticity dynamics diagnosis methods in the field of aerodynamic optimisation design of multi-stage compressor.

In this paper, vorticity dynamics theories are introduced into the flow field diagnosis of high-load counter-rotating compressor, the steady turbulent calculation is carried out at the design point, and the flow separation structures such as shock wave and secondary flow in the passage are diagnosed by vorticity dynamics, so as to find the part with poor local blade geometry. Based on the geometric optimisation platform built by the research group, the camber lines of the low-pressure rotor and high-pressure rotor are adjusted, and the improvement of compressor aerodynamic performance is verified by comparing the distribution characteristics of vorticity dynamics parameters on the blade surface before and after optimisation. In addition, based on the circumferential vorticity and BVF flow field diagnosis method, the boundary enstrophy flux (BEF) diagnosis method is developed. From the perspective of work and energy conversion of the compressor, the contribution of blade local geometric characteristics to the control of flow separation degree is analysed, which proves the practicability and advancement of vorticity dynamics diagnosis methods.

## 2.0 Vorticity dynamics theories

BVF is considered the root of multi-scale flow separation in the passage [31–33]. The essence of BVF diagnosis method is to express the forces and moments acting on the blade as the integral form of the first or second moment of BVF, by observing the distribution characteristics of BVF on the blade surface, the fluid’s positive or negative contribution regions to the blade moment can be directly determined.

The concept of BVF was first proposed by Lighthill [34]; this parameter represents the rate at which the vorticity diffuses into the fluid through viscous diffusion, and it describes the vorticity flux diffused through a unit area in unit time. It is an indispensable basic tool for studying the interaction between vorticity and wall. The equations are as follows:

$$\omega = \nabla \times u \tag{1}$$

$$\sigma = \frac{\partial(\mu\omega)}{\partial n} \tag{2}$$

Where  $\omega$  is the vorticity,  $\mu$  is the dynamics viscosity coefficient,  $n$  is the unit normal vector for wall. For three-dimensional viscous compressible flow, BVF consists of three parts:

$$\sigma = \sigma_a + \sigma_p + \sigma_\tau \tag{3}$$

It refers to  $\sigma_a$  produced by inertia force,  $\sigma_p$  produced by normal stress and  $\sigma_\tau$  produced by shear stress on the surface of the fluid, respectively.

$$\sigma_a = n \times a \tag{4}$$

$$\sigma_p = \frac{1}{\rho} n \times \nabla p \tag{5}$$

$$\sigma_\tau = \frac{1}{\rho} (n \times \nabla) \times (\mu\omega) \tag{6}$$

Where  $p$  is the pressure,  $\rho$  is the density.

The flow in the high-load counter-rotating compressor passage is dominated by high Reynolds number flow, and the order of magnitude of  $\sigma_\tau$  is much smaller than that of  $\sigma_p$ , which can be basically ignored in the flow analysis. The blade is in a uniform rotation state, and there is wall no slip, so BVF only needs to consider  $\sigma_p$  generated by normal stress. For the counter-rotating compressor, the normal stress is the pressure. The Equation (7) is as follows:

$$\sigma = \sigma_p = \begin{vmatrix} x & y & z \\ i & j & k \\ \partial p / \partial x & \partial p / \partial y & \partial p / \partial z \end{vmatrix} \quad (7)$$

The axial moment generated by the pressure gradient on the blade surface can be expressed as follows:

$$M_z = - \int_S (r \times pn)_z dS = - \frac{1}{2} \int_S \rho(r \cdot r) \sigma_{pz} dS + \frac{1}{2} \oint_{\partial S} \rho(r \cdot r) dz \quad (8)$$

Where  $s$  is the surface area of blade,  $\partial S$  is the boundary of blade surface,  $\sigma_{pz}$  is the axial component of  $\sigma_p$ .

It can be seen from Equation (8) that the first term on the right is the surface integral of  $\sigma_{pz}$  on the blade, and the second term on the right is the line integral of the pressure moment on the boundary. The  $\sigma_{pz}$  is shown in Equation (9), which is mainly related to the radial and circumferential pressure gradients and is the main reason for the formation of the passage vortex and radial secondary flow [35]. The axial moment is closely related to the net power of the compressor, Equation (10) gives the relationship between the net power and  $\sigma_{pz}$  on the blade surface, and it can be analysed that  $\sigma_{pz}$  positive peak will be detrimental to the net power. Therefore, BVF diagnosis only needs to focus on the distribution characteristics of  $\sigma_{pz}$  on the blade surface. For the convenience of writing, the BVF diagnostic method mentioned below diagnoses the distribution characteristics of  $\sigma_{pz}$  on the blade surface.

$$\sigma_{pz} = \frac{1}{\rho} \left( \frac{\partial p}{\partial y} i - \frac{\partial p}{\partial x} j \right) \quad (9)$$

$$L_u = -\Omega M_z = \Omega \left( -\frac{1}{2} \int_S \rho(r \cdot r) \sigma_{pz} dS + \frac{1}{2} \oint_{\partial S} \rho(r \cdot r) dz \right) \quad (10)$$

The vector lines of vorticity dynamics parameters can also predict the three-dimensional boundary layer separation phenomenon. When skin-friction vector  $\tau$ -lines on the blade surface converge, the BVF  $\sigma_p$ -lines turn basically along the direction of the skin-friction vector  $\tau$ -lines, that is, parallel to the skin-friction vector  $\tau$ -lines, and there is a positive peak of  $\sigma_{pz}$ , the flow in the nearby area will be separated. In addition, when skin-friction vector  $\tau$ -lines on the blade surface converge, and the curvature of the vorticity vector  $\omega$ -lines reach the local maximum value at the same time, it can also be determined that there is flow separation, which is the position that needs to be focused on optimised [36, 37]. The expression of the above theory is as follows:

$$\frac{\sigma_p \times \tau}{|\sigma_p| |\tau|} = b(\text{Re}^{-1/8}) \quad (11)$$

$$\tau = \mu \omega \times n \quad (12)$$

Where  $b(\text{Re}^{-1/8})$  is the value of  $\text{Re}^{-1/8}$  at a point on the blade surface.

Equation (11) shows that the angle between BVF  $\sigma_p$ -lines and the skin-friction vector  $\tau$ -lines is inversely proportional to Reynolds number, the smaller the Reynolds number, the larger the angle.

The surface integral of BVF on the non-rotating solid wall is always zero, which makes it impossible to use BVF diagnostic method to study how much vorticity diffuses into the fluid on a closed surface. Enstrophy is another important concept in vorticity dynamics theory, which is defined as a scalar  $0.5\omega^2$ . Its changes involve dynamics properties and kinematic properties, and it can be used to judge whether the flow field is swirling and the degree of swirling. The square of the vorticity in enstrophy can avoid that  $\omega$  in the closed vortex tube will offset each other when integrating. Based on the Navier-Stokes

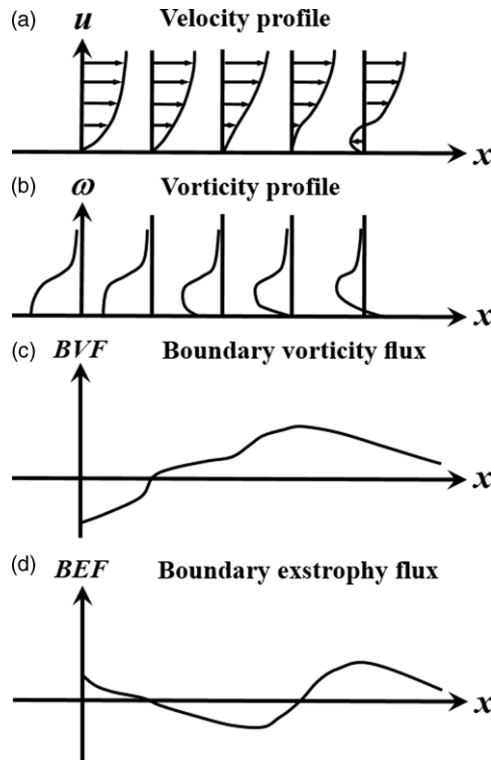


**Figure 1.** Parameter distribution of boundary layer during transition from attachment to separation. (a) velocity, (b) vorticity, (c) BVF and (d) BEF [37].

energy equation, it is analysed that enstrophy can reflect the energy dissipation characteristics of the fluid. Similar to the mathematical relationship of BVF, the normal gradient of enstrophy on the blade surface is the BEF, the co-analysis of BVF and BEF can comprehensively study the physical mechanism of vorticity entering the fluid from the boundary.

The definition formula of BEF is as follows:

$$\eta^* \equiv v \frac{\partial}{\partial n} \left( \frac{1}{2} \omega^2 \right) = \frac{1}{\rho} \omega \cdot \sigma \tag{13}$$

It can be seen that BEF and the projections of BVF along the vorticity direction are closely related. It can be concluded from the above Equation (13) that in some regions of wall, when  $\eta > 0$ , the direction of BVF and vorticity are the same. In this case, the shedding vorticity from the wall will increase the vorticity near the wall, and this area of wall is the vorticity source. When  $\eta < 0$ , the direction of BVF and vorticity are the opposite. In this case, the shedding vorticity from the wall will offset the vorticity near the wall, and this area of wall is the vorticity convergence.

Wu et al. [37] summarised the distribution laws of different parameters before and after flow separation in a two-dimensional plate boundary layer, as shown in Fig. 1. For the fluid flow with an adverse pressure gradient in the boundary layer, the sign of the BVF is opposite to the vorticity near the wall, the shedding vorticity from the wall will offset the original vorticity, and the continuous development of this situation will cause  $\partial u / \partial y$ , hence flow separation occurs according to Prandtl’s separation theory. It can be seen that the appearance of BVF positive peak is the sufficient condition for flow separation. In addition, when BEF goes from less than zero to greater than zero, airflow also starts to separate.

There is a direct mathematical relationship between the aerodynamic performance of the compressor and the circumferential vorticity, and the distribution of the circumferential vorticity directly affects

the flow state in the compressor passage [18]. Let  $S_1$ , and  $S_2$  denote inlet plane and outlet plane for compressor, respectively. The relationship between total pressure ratio and circumferential vorticity is as follows:

$$\pi = \frac{p_2^*}{p_1^*} = \frac{\int_{S_2} \rho u_z p^* dS}{\int_{S_1} \rho u_z p^* dS} = \frac{\int_{S_2} \rho u_z p^* dS}{\int_{S_1} \rho u_z p^* dS} = \frac{\int_{S_2} \rho u_z p^* dS}{C_1} = \frac{-\int_{S_2} r \rho p^* \frac{\partial u_z}{\partial r} dS}{2C_1} \approx \frac{\int_{S_2} r \rho p^* \omega_\theta dS}{C_2} \tag{14}$$

$$C_2 = 2C_1 = \int_{S_1} \rho u_z p^* dS \approx -0.5 \int_{S_1} r \rho p^* \frac{\partial u_z}{\partial r} dS = -\pi \int_{r_1}^{r_2} r^2 \rho p^* \frac{\partial u_z}{\partial r} dr \approx \pi \int_{r_1}^{r_2} r^2 \rho p^* \omega_\theta dr \tag{15}$$

where,  $C_1$  and  $C_2$  are constants at inlet plane of compressor,  $P^*$  is the total pressure,  $\omega_\theta$  is circumferential vorticity,  $u_z$  is the axial component of velocity,  $r$  is the radial position.

Using a similar method to the total pressure ratio, the relation of total temperature ratio by circumferential vorticity expression is written as follows:

$$T = \frac{T_2^*}{T_1^*} = \frac{\int_{S_2} \rho u_z T^* dS}{\int_{S_1} \rho u_z T^* dS} = \frac{\int_{S_2} \rho u_z T^* dS}{\int_{S_1} \rho u_z T^* dS} = \frac{\int_{S_2} \rho u_z T^* dS}{C_3} = \frac{-\int_{S_2} r \rho T^* \frac{\partial u_z}{\partial r} dS}{2C_3} \approx \frac{\int_{S_2} r \rho T^* \omega_\theta dS}{C_4} \tag{16}$$

$$C_4 = 2C_3 = \int_{S_1} \rho u_z T^* dS \approx -0.5 \int_{S_1} r \rho T^* \frac{\partial u_z}{\partial r} dS = -\pi \int_{r_1}^{r_2} r^2 \rho T^* \frac{\partial u_z}{\partial r} dr \approx \pi \int_{r_1}^{r_2} r^2 \rho T^* \omega_\theta dr \tag{17}$$

Where  $C_3$  and  $C_4$  are constants at inlet plane of compressor.  $T^*$  is the total temperature.

The compressor efficiency equation based on Equations (14–17) is as follows:

$$\eta = \frac{\left(\frac{p_2^*}{p_1^*}\right)^{\frac{\gamma-1}{\gamma}} - 1}{\frac{T_2^*}{T_1^*} - 1} = \frac{\pi_{\pi}^{\frac{\gamma-1}{\gamma}} - 1}{T_{\pi} - 1} \approx \frac{\left(\frac{\int_{S_2} r \rho p^* \omega_\theta dS}{C_2}\right)^{\frac{\gamma-1}{\gamma}} - 1}{\frac{\int_{S_2} r \rho T^* \omega_\theta dS}{C_4} - 1} \tag{18}$$

### 3.0 Calculation model and aerodynamic optimisation design platform

The object of diagnosis and optimisation design is a high-load counter-rotating compressor with a 1/2 + 1 aerodynamic configuration, and its geometric model is shown in Fig. 2. There are three rows of blades from the inlet to the outlet, which are low-pressure rotor (R1), high-pressure rotor (R2), and stator in turn. The three-dimensional fluid simulation software NUMECA is used for steady calculation. Among them, the Spalart-Allmaras model is selected as the turbulence model, which can accurately simulate the shock wave and separation phenomenon in the passage, and this turbulence model has been used by some scholars [37–40]. At the inlet, the total temperature is 288.15 K and the total pressure is 101325 Pa. At the outlet, the static pressure at the design point is 274 kPa. The numerical method verification are described in (41).

The geometric mesh division is completed in the NUMECA/AutoGrid5 module. The schematic diagram of meridional plane mesh is shown in Fig. 3. The O<sub>4</sub>H grid topology is selected. In order to accurately solve the internal flow of the boundary layer, the surface of the blade profile adopts the structured grid, and the height of the first layer of the grid is 0.005 mm. Due to the complex shock wave problem in the high-Mach-number compressor channel, the degree to which the number of grids affects the simulation results must be investigated. The results of the global parameter grid independence tests are shown in Table 1. When the grid number exceeds 2.4 million, the relative changes between the mass flow rate, total pressure ratio and adiabatic efficiency are all less than 0.1% at the design point, and the simulation results tend to be stable. In addition, Fig. 4 shows the isentropic Mach number of the 50%

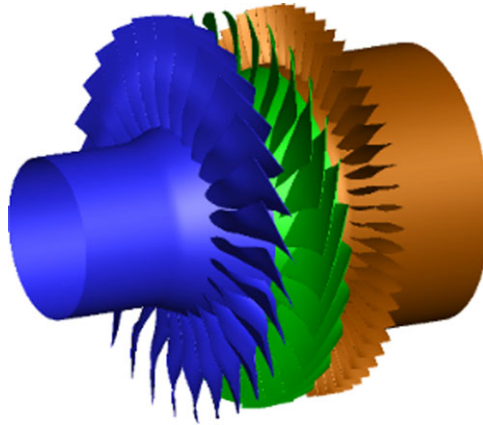


*Figure 2. Geometric model.*

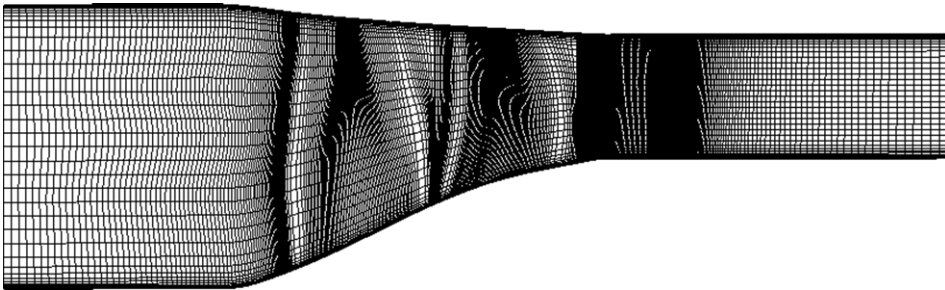


*Figure 3. The schematic diagram of the meridional plane mesh.*

span section of the R1 blade under different cases, and the results show that under different grid numbers, its value changes relatively little. Considering the computational cost, the case 4 grid parameter setting is adopted in all subsequent examples in this paper.

The aerodynamic optimisation design platform developed by the research group uses the numerical optimisation method based on an artificial neural network and genetic algorithm, and it is finally integrated on the NUMECA/Design3D module by coupling computational fluid dynamics technology and a self-edited Python script. The logical relationship is shown in Fig. 5. The user defined module can complete the functions of blade parametric modeling, grid division, physical model selection and boundary condition setting. The Python script in the multi-stage blade optimisation script module is the highlight of the highly automated platform, which first determines the blade geometric parameters that need to be modified and defines the geometric parameters as optimisation variables that the platform can recognise, and then completes the link of the geometry functions. Second, the method determines the range of optimisation variables, which are used to limit the parameter search space of the optimisation algorithm, and then interacts with the user defined module and the numerical optimisation module to complete the work of generating geometric files, perform grid generation and assembly of the meshes. The resulting grid is invoked by the solver of the numerical optimisation module, and the objective function is automatically obtained. For the effective samples generated by the numerical optimisation module, artificial neural networks can be used to find the relationship between the objective function and the optimisation variables, and then the optimal value of the objective function can be found through the genetic algorithm to obtain the optimal blade geometry.



**Table 1.** *Grid independence verification*

Case	Grid Distribution (Azimuthal × Spanwise × Streamwise)			Total Grid Cell Number	Performance Parameters		
	R1	R2	Stator		Efficiency	Total Pressure Ratio	Mass Flow Rate
1	37 × 65 × 121	37 × 65 × 121	41 × 49 × 121	1,058,009	85.46%	2.929	19.83
2	49 × 69 × 169	49 × 69 × 169	49 × 53 × 153	1,539,677	85.55%	2.928	19.84
3	53 × 73 × 161	53 × 73 × 161	49 × 57 × 161	1,956,273	85.61%	2.928	19.85
4	61 × 73 × 193	61 × 73 × 185	49 × 57 × 177	2,391,461	85.71%	2.928	19.85
5	61 × 77 × 193	61 × 77 × 201	49 × 61 × 193	2,730,073	85.72%	2.928	19.85



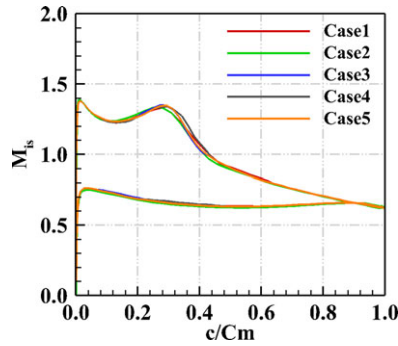


Figure 4. Isentropic Mach number.

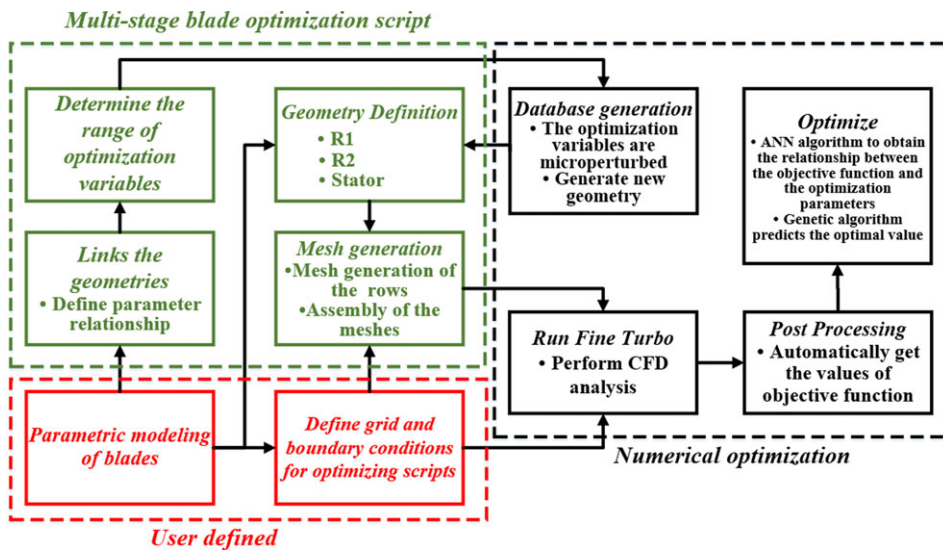
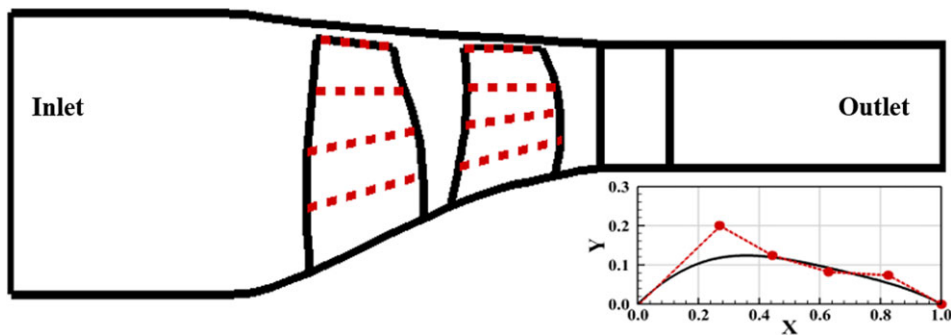


Figure 5. Aerodynamic optimisation design platform.

The parameterisation of camber line is shown in Fig. 6. To keep the leading-edge position of profile unchanged, the camber line is fitted with a high-order Bezier curve controlled by five discrete points, which can ensure a smooth blade profile and avoid large aerodynamic loss. Each blade has four parametric cross-sections equidistantly distributed along the spanwise direction. They are represented by the red dotted line in Fig. 6. The specific optimisation method is to add a perturbation amount to each discrete point of the camber line of the R1 and R2 blade designated sections, respectively, and optimise the three-dimensional blade channel geometry by controlling the shape of the camber line. The purpose of optimisation is to improve the compressor efficiency on the premise of ensuring the total pressure ratio. The focus of this paper is to study the application of vorticity dynamics theory in the flow field diagnosis and aerodynamic performance optimisation design of counter-rotating compressor. Therefore, the specific content of optimisation design will not be described too much. The optimisation process and results are described in (41).

#### 4.0 Results and discussions

The comparison of compressor aerodynamic performance characteristic lines before and after optimisation is shown in Fig. 7. After optimisation, the working range of the counter-rotating compressor



**Figure 6.** Parameterisation of camber line and the distribution of the sections.

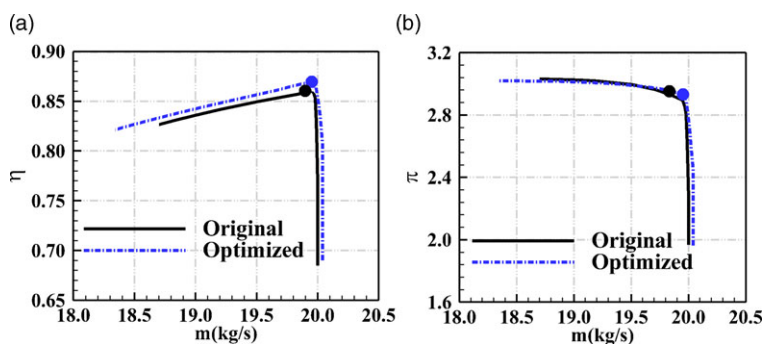


**Figure 7.** Aerodynamic performance characteristic lines; (a) adiabatic efficiency vs. mass flow rate and (b) total pressure ratio vs. mass flow rate.

is obviously increased. The efficiency of the compressor is significantly increased at both design and off-design points, and the comprehensive aerodynamic performance is improved. The aerodynamic performance parameters of the compressor at the design point are shown in Table 2. After optimisation, the compressor efficiency is increased by 1.16%.

#### 4.1 Conventional flow field analysis

The conventional flow field analysis method is to extract the distribution trend of static pressure and entropy on the blade surface in the post-processing, and qualitatively describes the movement characteristics of the gas and the overall quality of flow field before and after optimisation. Figures 8 and 9, respectively, show the distribution characteristics of static pressure and entropy on the suction surfaces of R1 and R2 blades before and after the optimisation of the camber lines at the design point. It can be seen from the static pressure map that the static pressure trend of the two blades increases from front to back along the flow direction. The static pressure changes greatly in the area near the middle of the blades, and there may be flow separation problems in the boundary layer. The entropy map shows that the above-left of R1 blade and the left of R2 blade have high entropy generation, and there is a local catastrophe phenomenon of entropy, indicating that there may be low-energy fluid accumulation at this location, which affects the efficient and stable operation of the counter-rotating compressor.

It is worth noting that there is no obvious difference in the distribution of static pressure and entropy on the suction surface of the two blades before and after optimisation, which has limited reference significance for quantitative analysis of the degree and range of fluid separation, and it is not possible to directly determine whether the aerodynamic performance optimisation is successful or not. The above

**Table 2.** Aerodynamic performance at the design point

Parameters		Original	Optimised
Efficiency( $\eta$ )	value	85.71%	86.87%
	%	0	+1.16%
PR( $\pi$ )	value	2.928	2.926
	%	0	-0.07%
Mass flow rate	value	19.85	19.95
	%	0	+0.5%

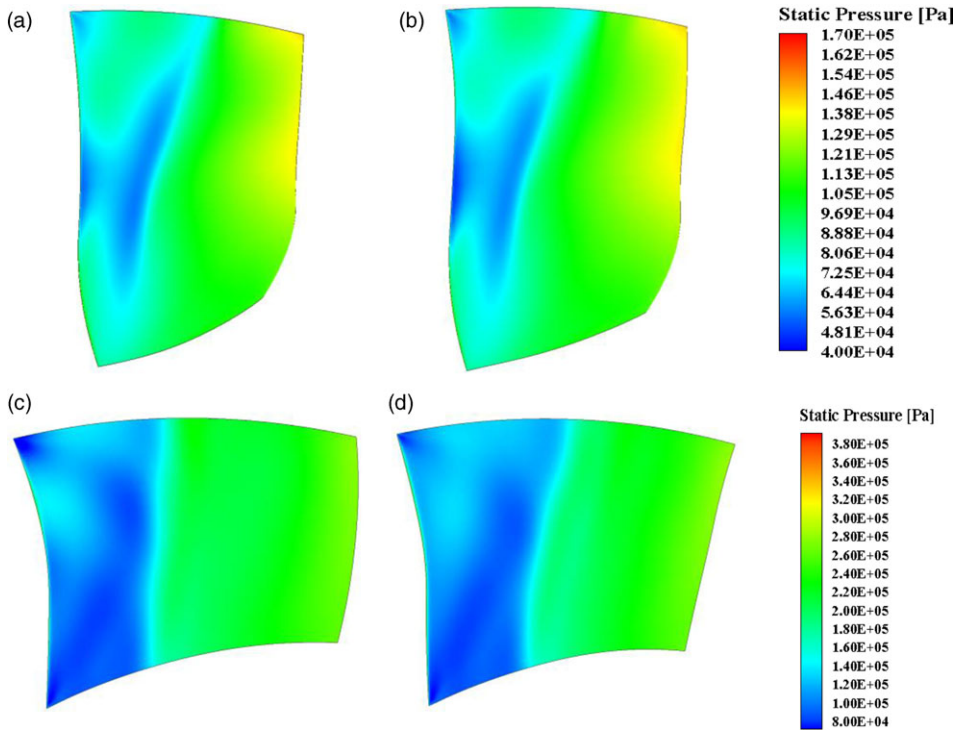


**Figure 8.** The distribution of static pressure on the blade suction surface; (a) original-R1, (b) optimised-R1, (c) original-R2 and (d) optimised-R2.

research indicates that the analysis method of flow field structure under the conventional framework of  $(v, p)$  has limitations, which cannot accurately predict and describe the complex vortices motion and flow separation in the passage of high-load counter-rotating compressor.

#### 4.2 Vorticity dynamics diagnosis

When the flow field parameters themselves cannot show too much useful information, we need to further analyse the derivative of flow parameters, which is very important for the aerodynamic optimisation design and flow field diagnosis of counter-rotating compressors, and this is also the fundamental reason for vorticity dynamics diagnosis from the perspective of velocity derivative and vorticity derivative. Under the framework of  $(\omega, \Pi)$ , the regions with negative contribution to aerodynamic performance in the compressor passage is diagnosed, and the flow separation is fundamentally controlled by optimising the geometric structure in the negative contribution region [42–44]. Figures 10 and 11 shows the

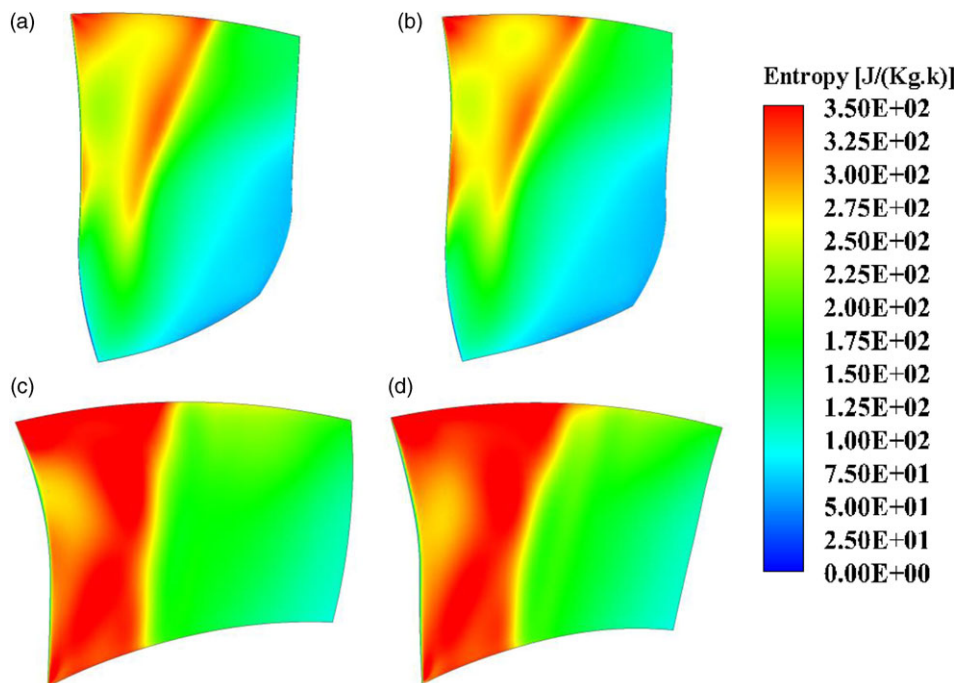


**Figure 9.** The distribution of entropy on the blade suction surface; (a) original-R1, (b) optimised-R1, (c) original-R2 and (d) optimised-R2.

comparative analysis of axial static pressure gradient, axial entropy gradient and the skin-friction vector  $\tau$ -lines on the suction surface before and after optimisation. Both blades have convergence region of skin-friction vector  $\tau$ -lines and the shock wave separation bubble is generated here. After optimisation, the axial pressure gradient and axial entropy gradient of both blades around the shock wave position are significantly reduced, the distribution characteristics of  $\tau$ -lines are greatly improved, the flow separation scale is significantly reduced, and the shock wave loss and the friction loss of boundary layer are reduced. In addition, in the middle of the leading edge of R1 blade, the matching state between the blade and the airflow becomes worse after optimisation. The static pressure gradient and entropy gradient diagnosis amplify the bad separation phenomenon in this area. The above research confirms that the derivation of flow parameters can better describe the quality of flow field than the parameters themselves, especially for the diagnosis and analysis of flow field with many vortices.

#### 4.2.1 BVF diagnosis of blade surface

BVF, as the derivative of the fundamental quantity, can amplify the adverse regions of the flow field, and directly reveal the problems and locations in the passage geometry. Combined with the physical meaning of BVF above, the separation degree of boundary layer can be judged more intuitively by comparing the BVF distribution on the blade suction surface before and after optimisation.

Figure 12 shows the distribution of BVF on the R1 and R2 blade suction surface before and after optimisation. For the flow in the high-load compressor passage, the region near BVF negative peak on the blade surface has a positive effect on the flow, the region near the BVF positive peak is usually accompanied by shock waves and vortices. A large positive BVF peak and the strong uneven BVF distribution are not conducive to the pressurisation by the rotor blades and high-efficiency operation. The results show that BVF can accurately capture the position and strength of the shock wave. After the optimisation of R1 blade, the distribution area of BVF positive peak near the shock wave is significantly reduced,



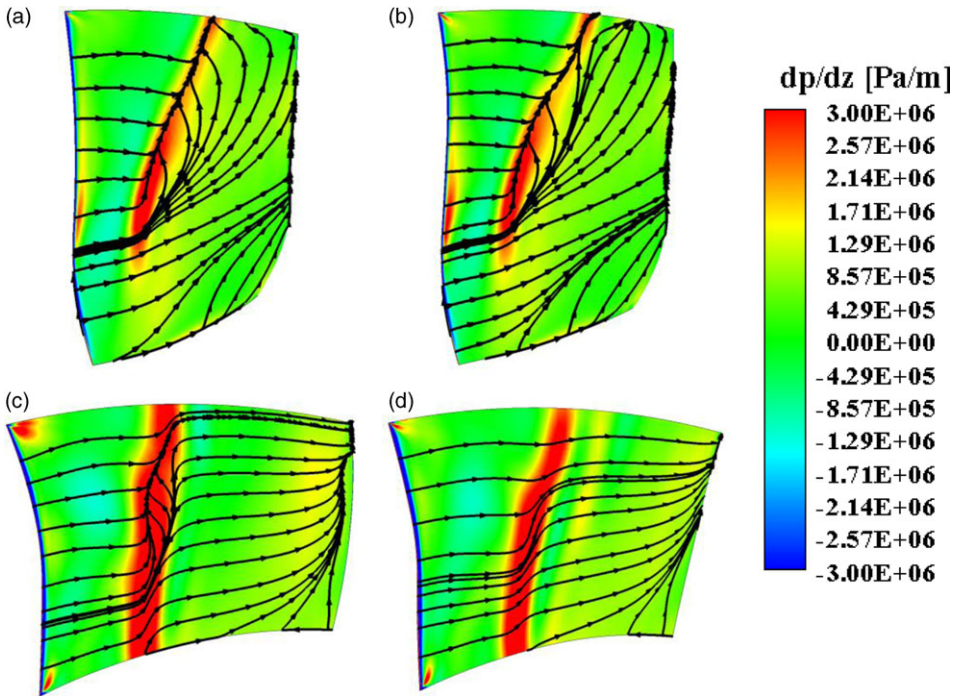


Figure 10. The distribution of axial static pressure gradient and the skin-friction vector  $\tau$ -lines; (a) original-R1, (b) optimised-R1, (c) original-R2 and (d) optimised-R2.

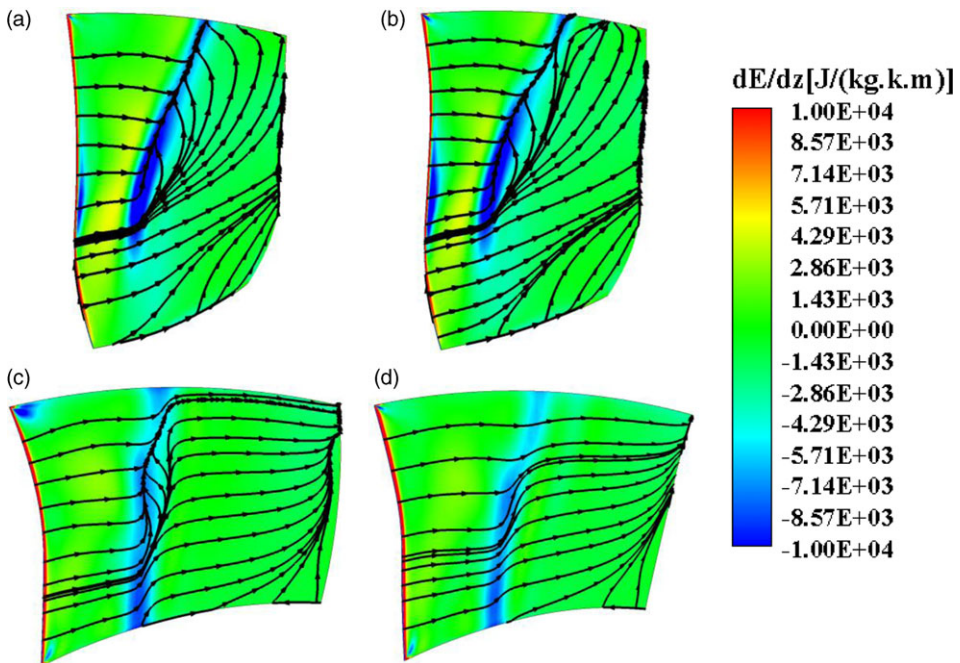
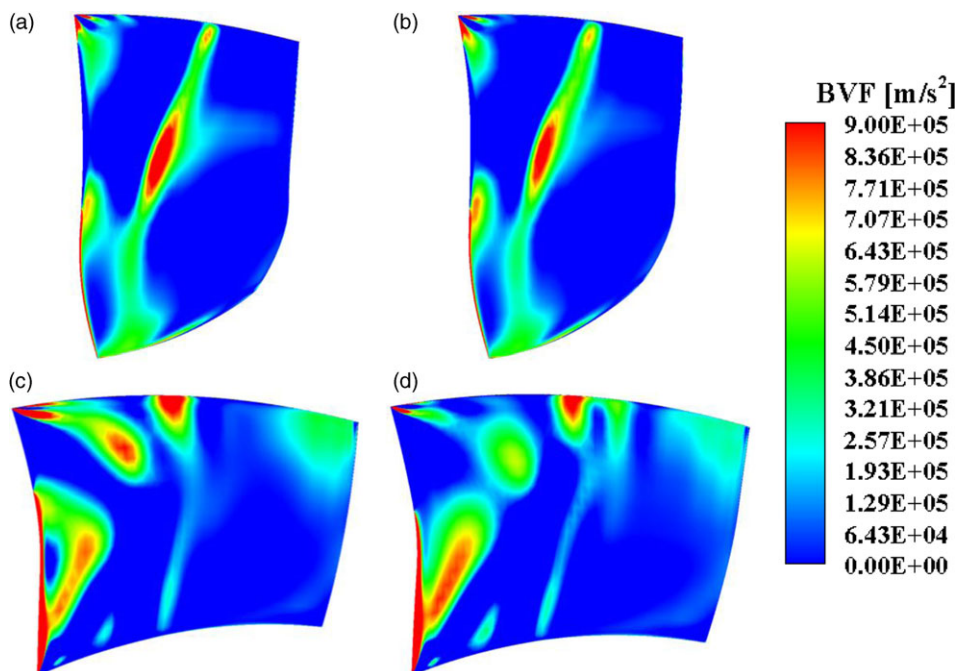


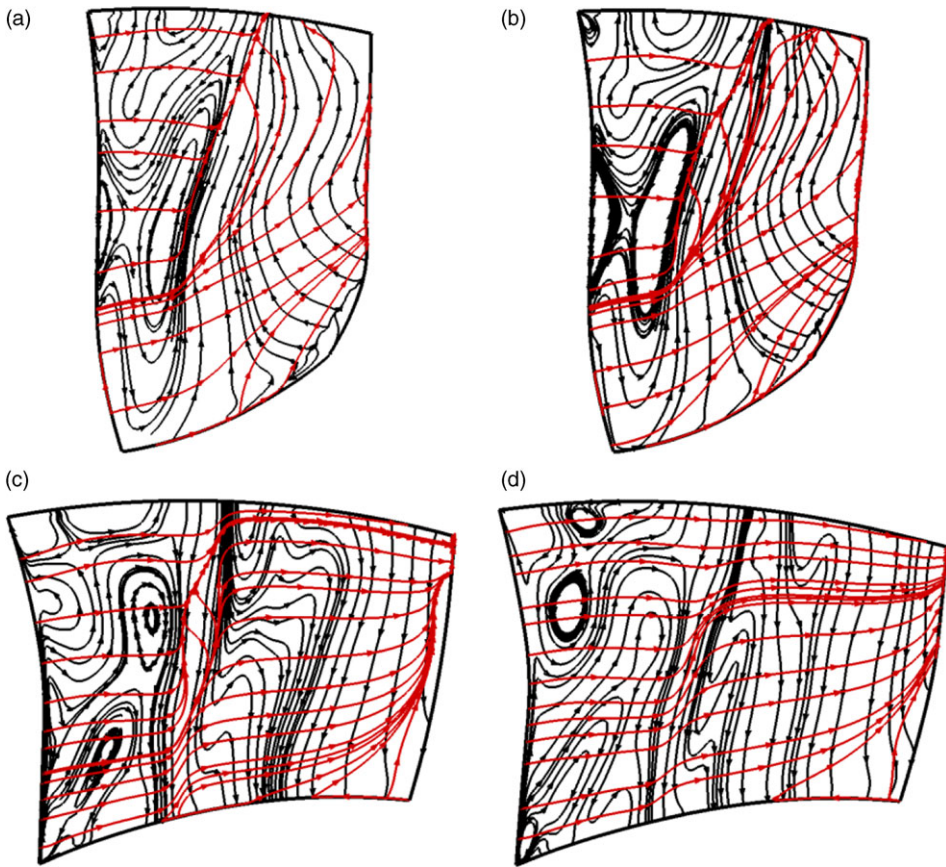
Figure 11. The distribution of axial entropy gradient and the skin-friction vector  $\tau$ -lines; (a) original-R1, (b) optimised-R1, (c) original-R2 and (d) optimised-R2.



**Figure 12.** The distribution of BVF on the blade suction surface; (a) original-R1, (b) optimised-R1, (c) original-R2 and (d) optimised-R2.

indicating that the pressure gradient decreases, the shock wave intensity decreases, then the airflow flow loss is reduced. In addition, the BVF positive peak region moves downstream along the flow direction and closer to the trailing edge, indicating that the shock wave position is inclined to the downstream of the blade, which is conducive to the compressor working under higher backpressure, and thus improves the stall margin of the compressor. The BVF map of R2 blade shows that the vortices generated by the tip clearance has a negative contribution to the airflow in the blade passage. After optimisation, the area of BVF positive peak decreases, which is conducive to improving compressor efficiency. It is worth noting that the areas of BVF positive peak and uneven distribution occur at the leading edge of both blades, which is the position where the blade and the fluid just contact, and the inlet stagger angle of the blade may be improperly designed, leading to fluid instability. The above results indicate that the control of BVF distribution is of guiding significance to the flow analysis and aerodynamic design of counter-rotating compressor.

Figure 13 shows the distribution of vector lines of  $(\tau, \sigma_p)$  on the R1 and R2 blade suction surface before and after optimisation. Among them, the red lines are  $\tau$ , the black lines are  $\sigma_p$ . The simulation results in this paper verify the theory of three-dimensional flow separation vortex on arbitrarily curved surfaces described in (45). Flow separation occurs in the area where BVF  $\sigma_p$ -lines are parallel to the skin-friction vector  $\tau$ -lines. The trend of BVF  $\sigma_p$ -lines distribution before and after R1 blade optimisation has little change. But after optimisation, the BVF  $\sigma_p$ -lines parallel to the skin-friction vector  $\tau$ -lines in the area near shock wave are more concentrated and radial BVF  $\sigma_p$ -lines descends in gradient indicating that the separation area is reduced, and the strength and influence range of shock wave become smaller. For the optimised R2 blade, the distribution characteristic of BVF  $\sigma_p$ -lines parallel to the skin-friction vector  $\tau$ -lines are more uniform in the middle of blade, and the BVF  $\sigma_p$ -lines parallel to skin-friction vector  $\tau$ -lines are shifted upward in the corner of the trailing edge, indicating that the strength of shock wave and secondary flow decreased correspondingly. These typical flow structures and characteristics show that the optimised rotor blades have excellent aerodynamic performance.



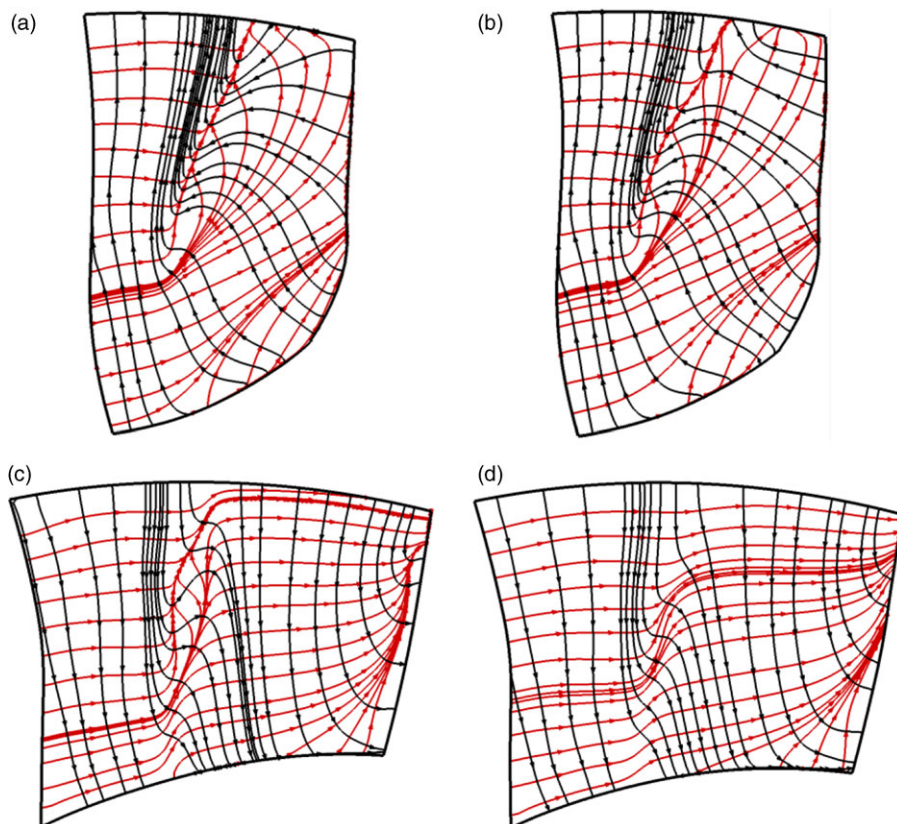
**Figure 13.** Vector lines of  $(\tau, \sigma_p)$  on blade suction surface; (a) original-R1, (b) optimised-R1, (c) original-R2 and (d) optimised-R2.

Figure 14 shows the distribution of vector lines of  $(\tau, \omega)$  on the R1 and R2 blade suction surface before and after optimisation. Among them, red lines are  $\tau$ , black lines are  $\omega$ . The skin-friction vector  $\tau$ -lines on R1 blade surface converge near the shock wave and in the corner region, and the vorticity vector  $\omega$ -lines are twisted here, and the curvature is larger than that in other regions, so flow separation can be determined there. After optimisation, the curvature of the vorticity vector  $\omega$ -lines in the separation region at the top of the tip decreases significantly, and the reduction of the separation scale means that the shock wave strength decreases. Similarly, the curvature of the vorticity vector  $\omega$ -lines in the middle of R2 blade surface are larger than that in other areas, which verifies the existence of shock wave here as well. The twist of the vorticity vector  $\omega$ -lines at the trailing edge of the blade indicates that there is secondary flow. After optimisation, the distribution of vorticity vector  $\omega$ -lines on the R2 blade surface is more uniform, the curvature of vorticity vector  $\omega$ -lines in the separation area decreases, and the degree of separation decreases.

#### 4.2.2 BEF diagnosis of blade surface

Figure 15 shows the distribution of vector lines of  $(\tau, \nabla p)$  and BEF on the R1 and R2 blade suction surface before and after optimisation. Among them, white lines are  $\nabla p$ , and black lines are  $\tau$ . The results show that the distribution of BEF is closely related to the distribution of pressure gradient  $(\nabla p)$ , the reason is that the theoretical formula of BEF described previously shows that the pressure gradient





**Figure 14.** Vector lines of  $(\tau, \omega)$  on blade suction surface; (a) original-R1, (b) optimised-R1, (c) original-R2 and (d) optimised-R2.

affects the distribution of BVF, and BVF affects the distribution of BEF. The BEF has a certain degree of accuracy for capturing the shock wave and the secondary flow in the passage, the separation bubble region on R1 blade surface induced by shock wave/boundary layer interaction has a positive BEF peak, and the size and range of separation bubble described by BEF are consistent with that described by the skin-friction vector  $\tau$ -lines. The unique pre-compressed profile on the above-left of R1 blade slows down the airflow in this area, forming a BEF negative peak. The distribution of BEF on the R2 blade surface is confused, but the prediction of separation bubble and secondary flow at the trailing edge is accurate, but it is accurate to predict the strength of the separation bubble and the secondary flow at the trailing edge. After optimisation, the BEF distribution of the two blades is more uniform, which indicates that the shock wave strength and energy dissipation decrease, and the energy exchange between fluid and blade is enhanced. Based on the above research results, the distribution characteristics of BEF on the blade surface can provide an improvement direction for improving the quality of flow field and aerodynamic performance of counter-rotating compressor.

#### 4.2.3 Circumferential vorticity diagnosis

Circumferential vorticity is the dynamics source that determines the flow capacity of the passage. By controlling the distribution characteristics of circumferential vorticity in the flow field, the balance can be obtained between the required lift force and the undesired drag force, which can make the counter-rotating compressor obtain the optimal aerodynamic performance. Figure 16 shows the circumferential

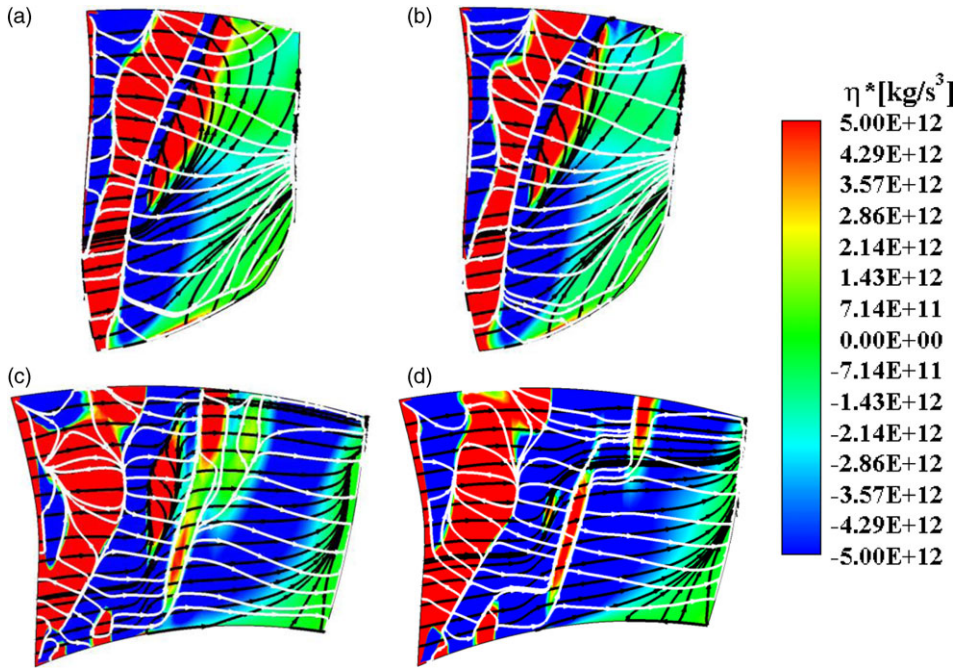


Figure 15. The distribution of BEF and vector lines of  $(\tau, \nabla p)$  on blade suction surface; (a) original-R1, (b) optimised-R1, (c) original-R2 and (d) optimised-R2.

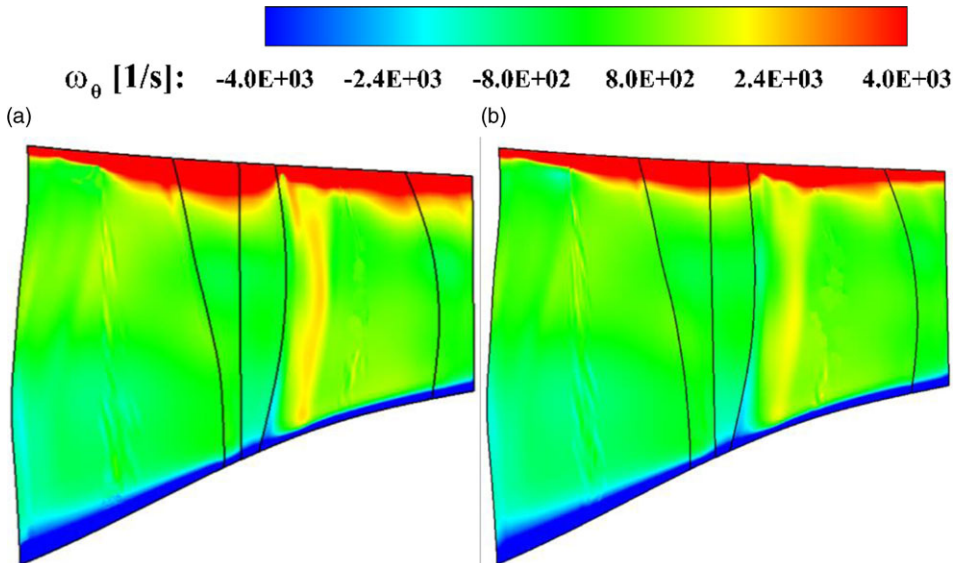
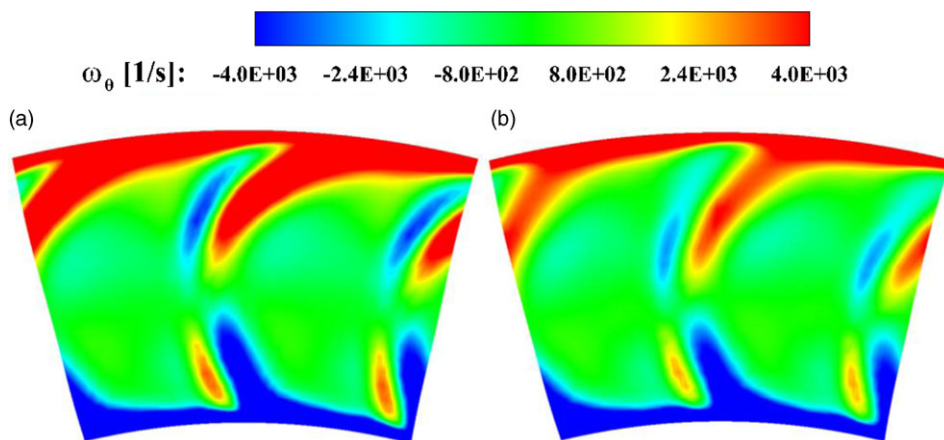


Figure 16. The circumferential vorticity distribution of the meridional plane; (a) original and (b) optimised.



**Figure 17.** The circumferential vorticity distribution of the cross-section at R2 blade outlet; (a) original and (b) optimised.

vorticity distribution map of the meridional plane. A large range of positive peak appeared in the tip area and a large range of negative peak appeared near the hub. Figure 17 shows the circumferential vorticity distribution map of the cross-section at R2 blade outlet. There is a circumferential vorticity positive peak in the tip area, and a large number of positive vorticities are mixed into the main flow, which is the result of the combined action of tip leakage vortex and boundary layer separation. There are negative vorticities mixed into the main flow near the hub, which is mainly caused by the secondary flow in the corner. The circumferential vorticity can reflect the high flow loss area near the wall. Based on the mathematical connection between the circumferential vorticity and compressor performance described above, the optimal distribution principle is that the positive and negative peak of circumferential vorticity should be confined to the near wall as far as possible to avoid diffusion to the main flow, thus causing large flow loss [46, 47]. After optimisation, the results show that the circumferential vorticities of the meridional surface and the cross-section at R2 blade outlet flow to the main flow area are suppressed, the flow capacity of the passage is enhanced, and the compressor efficiency is increased, which verifies the applicability of the principle of optimal distribution of circumferential vorticity to the optimisation design of counter-rotating compressor.

## 5.0 Conclusions

This paper describes the theories and diagnostic methods of vorticity dynamics and analyses the corresponding relationship between the flow field quality of counter-rotating compressor and vorticity dynamics parameters. The diagnostic methods of BVF, BEF and circumferential vorticity are explained respectively, and the application of the above methods in aerodynamic performance evaluation is introduced.

The circumferential vorticity diagnosis method based on vorticity dynamics mechanism is better than the conventional flow field diagnosis method. This paper presents the optimal distribution law of circumferential vorticity and verifies its practicability in the flow field diagnosis of high-load counter-rotating compressor, which provides a new solution for compressor optimisation design.

The BVF positive peak area is the direct reflection of shock wave or negative contribution area on the blade surface. The distribution characteristics of the BVF positive peak reflect the degree of flow turbulence caused by shock wave/boundary layer interaction and secondary flow. Weakening the distribution range of the BVF positive peak is an important means to improve the aerodynamic performance of the counter-rotating compressor.

The BEF diagnosis can be used as a new vorticity dynamics diagnosis method to evaluate and optimise the flow field performance and aerodynamic performance of counter-rotating compressor, and this parameter has a certain ability to capture high energy loss areas such as shock wave and secondary flow. By comparing the BEF distribution characteristics of the blade suction surface before and after optimisation, it is proved that the theory that this parameter can predict the performance of energy exchange between fluid and boundary is credible.

**Acknowledgements.** This research was funded by the National Science and Technology Major Project (J2019-II-0016-0037).

## References

- [1] Sun S., Wang S., Zhang L., *et al.* Design and performance analysis of a two-stage transonic low-reaction counter-rotating aspirated fan/compressor with inlet counter-swirl[J]. *Aerosp. Sci. Technol.*, 2021, **111**, (3), p 106519.
- [2] Khaleghi H., Shahriyari M.J., Heinrich M. A theory for rotating stall in contra-rotating fans:[J]. *Proc. Inst. Mech. Eng., Part C: J. Mech. Eng. Sci.*, 2021, **235**, (18), pp 3764–3773.
- [3] Liang T., Liu B., Spence S., *et al.* Numerical analysis of the effects of circumferential groove casing suction in a counter-rotating axial flow compressor:[J]. *Proc. Inst. Mech. Eng., Part A: J. Power Energy*, 2021, **235**, (5), pp 944–955.
- [4] Song W., Zhang Y., Chen H., *et al.* Transonic compressor blade optimization integrated with circumferential groove casing treatment[J]. *J. Turbomach.*, 2018, **141**, (3), p 031015.
- [5] Zhu J., Cai X., Ma D., *et al.* Improved structural design of wind turbine blade based on topology and size optimization[J]. *Int. J. Low-Carbon Technol.*, 2021, **17**, 69–79.
- [6] Wang H., Jiang X., Chao Y., *et al.* Numerical optimization of horizontal-axis wind turbine blades with surrogate model:[J]. *Proc. Inst. Mech. Eng., Part A: J. Power Energy*, 2021, **235**, (5), pp 1173–1186.
- [7] Krasnyk A.M. and Russky E.Y. Optimizing design parameters of rotating blades of mine axial fans [J]. *Interexpo GEO-Siberia*, 2020, **2**, pp 98–102.
- [8] Meng R. and Xie N.G. A competitive-cooperative game method for multi-objective optimization design of a horizontal axis wind turbine Blade[J]. *IEEE Access*, 2019, PP, (99), p 1.
- [9] Wang J.S. and Wang J.J. Vortex dynamics for flow around the slat cove at low Reynolds numbers[J]. *J. Fluid Mech.*, 2021, **919**, A27.
- [10] Moore X.X. and Richardson Y.Y. Skewed boundary layer flow near end walls of a compressor cascade[J]. *ASME J. Eng. Gas Turbines Power* 1957, **79**, pp 1789–1800.
- [11] Horlock J.H., Louis J.F., Percival P.M.E., *et al.* Wall stall in compressor cascades[J]. *J. Basic Eng.*, 1966, **88**, (3), pp 637–648.
- [12] Kan X., Wu W. and Zhong J. Effects of vortex dynamics mechanism of blade-end treatment on the flow losses in a compressor cascade at critical condition[J]. *Aerosp. Sci. Technol.*, 2020, **102**, (7), p 105857.
- [13] Wu J.Z., Lu X.Y., Denny A.G., *et al.* Post-stall flow control on an airfoil by local unsteady forcing[J]. *J. Fluid Mech.*, 1998, **371**, pp 21–58.
- [14] Wu X.H., Wu J.Z. and Wu J.M. Effective vorticity-velocity formulations for three-dimensional incompressible viscous flows[J]. *J. Comput. Phys.*, 1995, **122**, (1), pp 68–82.
- [15] Wu J.Z., Wu X.H. and Wu J.M. Streaming vorticity flux from oscillating walls with finite amplitude[J]. *Phys. Fluids A*, 1993, **5**, (8), pp 1933–1938.
- [16] Wu J.C. A theory for aerodynamic forces and moments[J]. *Theory Aerodyn. Forces Moments*, 1978, pp 1–58.
- [17] Wu J.C. Theory for aerodynamic force and moment in Viscous Flows[J]. *AIAA J.*, 1981, **19**, (4), 432–441.
- [18] Wu J.C. *Elements of Vorticity Aerodynamics[M]*. Beijing: Beijing Tsinghua University Press, 2005.
- [19] Lambert A.R. and Yarusyevych S. Characterization of vortex dynamics in a laminar separation bubble[J]. *AIAA J.*, 2014, **136**, (7), p 071101.
- [20] Wu J.Z. and Wu J.M. Boundary vorticity dynamics since lighthill’s 1963 Article: Review and development[J]. *Theor. Comput. Fluid Dyn.*, 1998, **10**, (1–4), pp 459–474.
- [21] Wu J.Z., Wu J.M. Vorticity dynamics on boundaries[J]. *Adv. Appl. Mech.*, 1996, **32**, (08), pp 119–222.
- [22] Wu J., Roach R., Lo C., *et al.* Dynamics diagnostics and design based on boundary vorticity dynamics[C]. *17th Applied Aerodynamics Conference*, American Institute of Aeronautics and Astronautics, 1999.
- [23] Wu J.Z. Interactions between a solid surface and a viscous compressible flow field[J]. *J. Fluid Mech.*, 1993, **254**, (-1), pp 183–211.
- [24] Li Q. and Guo M. Diagnostic and design approach of axial compressor based on local dynamics[J]. *Prog. Nat. Sci.*, 2005, **15**, (2), 221–228.
- [25] Ming G., Li Q., Hou A., *et al.* A diagnostic and design approach of axial compressor based on local dynamics[C]. *ASME Turbo Expo: Power for Land, Sea, & Air*, Barcelona, 2006, pp. 423–433.
- [26] Li F., Fan H., Wang Z., *et al.* Coupled design and optimization for runner blades of a tubular turbine based on the boundary vorticity dynamics theory[C]. *ASME-JSME-KSME 2011 Joint Fluids Eng. Conf.*, Shizuoka, 2011, pp 603–609.
- [27] Prashanth M.N. *Dynamics of Tip Leakage Vortex in a Transonic Fan[D]*. Lawrence, KS: University of Kansas, 2018.
- [28] Yang L., Fan H. and Chen N. Bidirectional flow diagnosis to optimize the design of a pump-turbine runner using vorticity dynamics theory[J]. *J. Tsinghua Univ. (Sci. Technol.)*, 2007, **5**, 686–690.



- [29] Zhang L., Liu S. and Wu Y. Vorticity dynamics analysis of flow field in Francis runner[J]. *J. Hydroelectr. Eng.*, 2007, **26**, (6), pp 106–110.
- [30] Honggang F., Naixiang C. and Lin Y. Three dimensional flow diagnosis of the pump turbine runner based on the dynamic vorticity[J]. *J. Hydroelectr. Eng.*, 2007, **26**, (3), pp 124–128.
- [31] Lu G., Li D., Zuo Z., et al. A boundary vorticity diagnosis of the flows in a model pump-turbine in turbine mode[J]. *Renew. Energy*, 2020, **153**, pp 1465–1478.
- [32] Li D.Y., Gong R.Z., Wang H.J., et al., Analysis of vorticity dynamics for hump characteristics of a pump turbine model, *J. Mech. Sci. Technol.*, 2016, **30**, (8), p 3641e3650.
- [33] Peng Z., Ouyang H., Wu Y., et al. Diagnosis and design improvement of the internal flow field in an automotive cooling fan based on boundary vorticity dynamics, part I: blade profile scaling and rotation. *J. Therm. Sci.*, 2022. doi: [10.1007/s11630-022-1663-0](https://doi.org/10.1007/s11630-022-1663-0)
- [34] Lighthill M.J. *Laminar Boundary Layer*[M]. Oxford: Oxford University Press, 1963, pp 46–113.
- [35] Wu H. and Jiang H.D. Theory and analysis method based on vorticity dynamics for gas turbine compressor[J]. *J. Aerosp. Power*, 2013, **28**, (4), pp 903–910.
- [36] Zhang J., Cai S., Li Y., et al. Optimization design of multiphase pump impeller based on combined genetic algorithm and boundary vortex flux diagnosis[J]. *J. Hydrodyn.*, 2017, **29**, (6), pp 1023–1034.
- [37] Wu J.Z., Ma, H.Y. and Zhou M.D. *Vorticity and Cortex Dynamics*. New York: Springer, 2006.
- [38] Rao J., Yuan W, Li Q., et al. Application of BVF diagnosis on unsteady rotor/stator matching [J]. *J. Aerosp. Power*, 2007, **22**, (7), 1082–1086.
- [39] Ming G., Xiaoyu Z., Sheng Z., et al. BVF application on blowing control of flow separation of a compressor cascade [J]. *J. Aerosp. Power*, 2008, **23**, (8), 1498–1503.
- [40] Li Q., Wu H, Guo M., et al. Vorticity dynamics in axial compressor flow diagnosis and design—Part II: Methodology and application of boundary vorticity flux[J]. *J. Fluids Eng.*, 2009, **132**, (1), pp 11102–11102.
- [41] Yan T., Chen H., Fang J. and Yan P. Research on 3d design of high-load counter-rotating Compressor based on aerodynamic optimization and CFD coupling method. *Energies*, 2022, **15**, p 4770.
- [42] Delery J. and Meauze G. A detailed experimental analysis of the flow in a highly loaded fixed compressor cascade: the iso-cascade cooperative program on code validation [J]. *Aerosp. Sci. Technol.*, 2003, **7**, (1), 1–9.
- [43] Müller R., Sauer H., Vogeler K., et al. Influencing the secondary losses in compressor cascades by a leading edge bulb modification at the endwall[R]. *ASME-GT2002-30442*.
- [44] Kan X.X., Lu H.W. and Zhong J.J. Topological characterization of vortex structures on a transonic compressor stator during the stalling process[J]. *Proc. Inst. Mech. Eng., Part G: J. Aerosp. Eng.*, 2016, **230**, (3), 566–580.
- [45] Wu J.Z., Tramel R.W., Zhu F.L. and Yin X.Y. A vorticity dynamics theory of three-dimensional flow separation [J]. *Phys. Fluids*, 2000, **12**, (8), pp 1932–1954.
- [46] Chen H., Turner M.G., Siddappaji K., et al. Vorticity dynamics based flow diagnosis for a 1.5-stage high pressure compressor with an optimized transonic rotor[C]. *ASME Turbo Expo*. Seoul, 2016, pp 1–12.
- [47] Yang Y., Wu H., Li Q., et al. Vorticity dynamics in axial compressor flow diagnosis and design [C]. In *ASME Turbo Expo 2007: Power for Land, Sea, and Air vol. 6 pt. A. Institute of Engineering Research, Peking University Beijing, 100871, People's Republic of China, 2007*, pp 147–158.